

The development of an augmented machine learning approach for the additive manufacturing of thermoelectric materials

Connor V. Headley^a, Roberto J. Herrera del Valle^a, Ji Ma^{a,*}, Prasanna Balachandran^{a,b}, Vijayarabathi Ponnambalam^c, Sania LeBlanc^c, Dylan Kirsch^{d,e}, Joshua B. Martin^d

^a Department of Materials Science and Engineering, University of Virginia, Charlottesville, Virginia 22903, USA

^b Department of Mechanical and Aerospace Engineering, University of Virginia, Charlottesville, Virginia 22903, USA

^c Department of Mechanical and Aerospace Engineering, George Washington University, Washington D.C. 20052, USA

^d Material Measurement Laboratory, National Institute of Standards and Technology (NIST), Gaithersburg, MD 20899, USA

^e Department of Materials Science & Engineering, University of Maryland, College Park, MD 20742, USA

ARTICLE INFO

Keywords:

Additive manufacturing
Laser powder bed fusion
Thermoelectric materials
Bismuth telluride
Machine learning
Processing maps

ABSTRACT

Through the integration of machine learning (ML) techniques alongside additive manufacturing (AM) experimentation, we demonstrate an iterative process to rapidly predict laser-material interactions and melt pool geometries throughout the build parameter space for a bismuth telluride thermoelectric (TE) material. In doing so, we determined process parameters that created crack-free, highly dense (>99 %) n-type bismuth telluride ($\text{Bi}_2\text{Te}_{2.7}\text{Se}_{0.3}$) parts through laser powder bed fusion (LPBF). Further, the ML-assisted understanding of the processing space allowed for the identification of build parameters that successfully yielded geometrically enhanced $\text{Bi}_2\text{Te}_{2.7}\text{Se}_{0.3}$ parts with reduced build times and no increase in experimental effort.

1. Introduction

A clear and present danger exists in our excessive and inefficient use of non-renewable fossil fuels. Rapid global industrialization has yielded an ever-increasing demand for electricity, which has so far been met through a commensurate rise in the burning of fossil fuels and emission of greenhouse gases [1]. Globally, about two-thirds of produced energy is lost as unutilized heat into the atmosphere [2,3]. Therefore, the need to improve localized cooling technologies [4] and recapture wasted heat energy in the form of usable electricity has both economic and environmental advantages. Thermoelectric (TE) materials have garnered interest over the past several decades as a potential solution to this crisis due to their ability to convert between heat and electrical energy directly and reversibly and offer a unique opportunity to reduce industrial and automobile heat waste [1,2,5,6]. However, their widespread adoption has been hindered by their low conversion efficiency ($\approx 5\%$) and high production cost [7–9].

When a temperature gradient is applied across a TE material, the more energetic charge carriers on the hot side will diffuse to the cold side, generating a proportional voltage. This phenomenon is known as

the Seebeck effect, one of three thermoelectric effects [7,10]. The conversion efficiency of a TE material can be qualitatively evaluated by the dimensionless figure of merit $ZT = (\sigma S^2/\kappa)T$, where σ is the electrical conductivity, S is the Seebeck coefficient, κ is the combined lattice and phonon thermal conductivities, and T is the temperature [7,10,11]. TE materials are most often assembled into devices known as TE modules, which are composed of many TE unicouples arranged thermally in parallel and electrically in series. Each TE unicouple consists of a grouped pair of n-type and p-type units called TE legs, as shown in Fig. 1. These modules are not only capable of using the Seebeck effect to convert between thermal and electrical energy, but they also have the advantages of being noise-free, pollution-free, and solid-state with no moving parts [1,12].

V_2VI_3 compounds (V = Group V elements Sb and Bi; VI = Group VI elements S, Se, and Te) have been the cornerstone TE materials, finding roles in both research and industrial settings due to their high TE figure of merit at room temperature [13,14]. Bismuth telluride (Bi_2Te_3) is the most commonly used V_2VI_3 compound [14]. For this study, a selenium-doped bismuth telluride ($\text{Bi}_2\text{Te}_{2.7}\text{Se}_{0.3}$) was used because of its clear n-type character, whereas binary bismuth telluride (Bi_2Te_3) can vary in its

* Corresponding author.

E-mail addresses: cvh3ba@virginia.edu, headley@virginia.edu (C.V. Headley), rjh6tug@virginia.edu (R.J. Herrera del Valle), jm5bu@virginia.edu, jm@virginia.edu (J. Ma), pvb5e@virginia.edu (P. Balachandran), sleblanc@email.gwu.edu (S. LeBlanc), dylan.kirsch@nist.gov (D. Kirsch), joshua.martin@nist.gov (J.B. Martin).

<https://doi.org/10.1016/j.jmpro.2024.02.045>

Received 3 October 2023; Received in revised form 24 January 2024; Accepted 19 February 2024

1526-6125/© 2024 The Society of Manufacturing Engineers. Published by Elsevier Ltd. All rights reserved.

character based upon the manufacturing process [13–15].

Additive manufacturing (AM) has emerged as a promising new approach to creating better TE devices [16]. Prior modeling work has shown that TE legs with more complex geometries and non-uniform cross-sectional areas result in larger thermal gradients and higher power generation potential than standard rectangular prism legs [7,17,18]. This would increase the effective, system-level ZT and conversion efficiency of the TE parts. Fig. 2 shows simulation results that demonstrate the predicted impact of hollow and trapezoidal geometries on thermal resistance when compared to a more traditional, rectangular TE leg. Unfortunately, the limitations of traditional TE manufacturing techniques restrict the possible geometries of TE legs to simple cuboids and cylinders. In contrast, AM techniques allow for the fabrication of more complex geometries, such as those shown in Fig. 2.

While many AM techniques exist, laser powder bed fusion (LPBF) was selected in this study due to its ability to create free form geometries and potentially reduce cost through the minimization of material waste and manufacturing steps [7]. LPBF is a non-equilibrium process that features rapid heating and cooling by using a laser beam to selectively melt thin, successive layers of powder particles [19]. This layer-by-layer construction can be utilized to produce fully dense, three-dimensional parts in complex geometries that are difficult to achieve through conventional manufacturing [12]. The primary input build parameters for the LPBF process involve the laser beam and are summarized in the input energy density (IED) [in J/cm^2] equation: $IED = p/(v d)$, where p is the laser power, v is the laser scan speed, and d is the laser beam diameter ($D4\sigma$) [20]. Other key parameters are the layer thickness (t) and hatch spacing (h), which is the distance between adjacent laser scans.

Multiple groups have previously worked on the AM of TE parts to take advantage of these benefits [10,12,21]. In 2018, Zhang et al. [19] demonstrated the first successful LPBF of a three-dimensional bismuth telluride (Bi_2Te_3) part with TE properties comparable to those created through traditional manufacturing methods. However, a lack of optimized build parameters produced a low final part relative density of 88 %. Additionally, these parts were made in simple cylinders and bars like those already being built using traditional manufacturing methods.

It is our belief that high densities in LPBF-built bismuth telluride parts can be achieved through process optimization. In doing so, the successful construction of bismuth telluride parts in more complex geometries can be achieved. Traditionally, AM process optimization for a new material requires extensive and time-consuming experimentation. A complementary approach using machine learning (ML) could potentially accelerate the understanding of the entire material processing space using fewer experiments and fewer data points. More specifically, our interest is in augmenting human intuition with predictions (along with the associated uncertainties) from ML models such that the human-ML interaction will lead to efficient navigation of the LPBF processing space. This is especially important in problems where one seeks to adopt LPBF-based techniques to rapidly optimize high quality parts of a novel

material whose thermophysical properties (e.g., latent heat of phase transformations, temperature-dependent thermal conductivity, specific heat capacity, density, etc.) are not known or well-studied. Lack of thermophysical data precludes the use of numerical models to inform the experimental approach.

Prior works have demonstrated the successful implementation of iterative Bayesian optimization and active (or adaptive) learning methods to AM systems. A vast majority of the effort has relied on constructing surrogate models to mimic the predictions of either simple (e.g., Eagar-Tsai model) and/or complex numerical models (e.g., finite element analysis) [22–25]. Subsequently, these surrogate models have guided the AM process space exploration. However, there are very few efforts dedicated to the construction of surrogate models for AM experiments (without the intermediate physical models). For example, Ye et al. [26] employed Bayesian optimization to identify the optimal processing parameters to fabricate high-density NiTi samples using the LPBF process. The authors started with nine samples to train the ML model and added three more samples (one sample per iteration) in a sequential manner as guided by the Bayesian optimization algorithm. In another study, Kitano et al. [27] discussed the use of Bayesian optimization method to identify the optimal laser irradiation conditions of Hastelloy X. More recently, Agarwal et al. [28] demonstrated the promise of classification learning methods to identify key processing parameters and *in-situ* sensor features that will result in a high power factor for LPBF-processed Bi_2Te_3 . Although this work is strictly not active learning, it demonstrates the growing interest in adopting data-driven ML methods to guide LPBF processing of complex materials.

In the present work, the principles borrowed from Bayesian optimization and active learning are leveraged to efficiently navigate the LPBF processing space. One of the key outcomes is the development of an understanding of the melt pool geometry trends (in terms of width and depth) as a function of laser power and scan speed. At the end of every ML training iteration, two maps are generated (both as functions of laser power and scan speed): 1) the ML predictions of melt pool width and depth and 2) the associated uncertainties in the ML predictions that collectively capture the total variation due to sampling, ML model bias, and inherent process uncertainties. These maps are consequently used as a guide to select the next set of LPBF conditions. It is important to note that the trained ML models do not recommend specific LPBF conditions, but instead augment the LPBF-based insights for ultimate decision making. As a result, the data-driven ML strategy is best described as augmented ML. The LPBF experimental efforts in turn use the knowledge gained from ML augmented single-track experiments to rapidly optimize LPBF process parameters capable of building highly dense, crack-free bismuth telluride parts in the nonstandard geometries that have been predicted to yield higher thermoelectric performance.

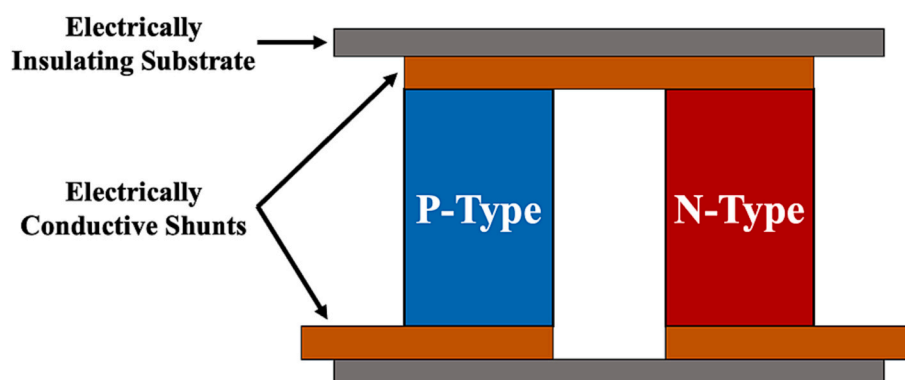


Fig. 1. Schematic of a typical thermoelectric uncouple (not to scale).

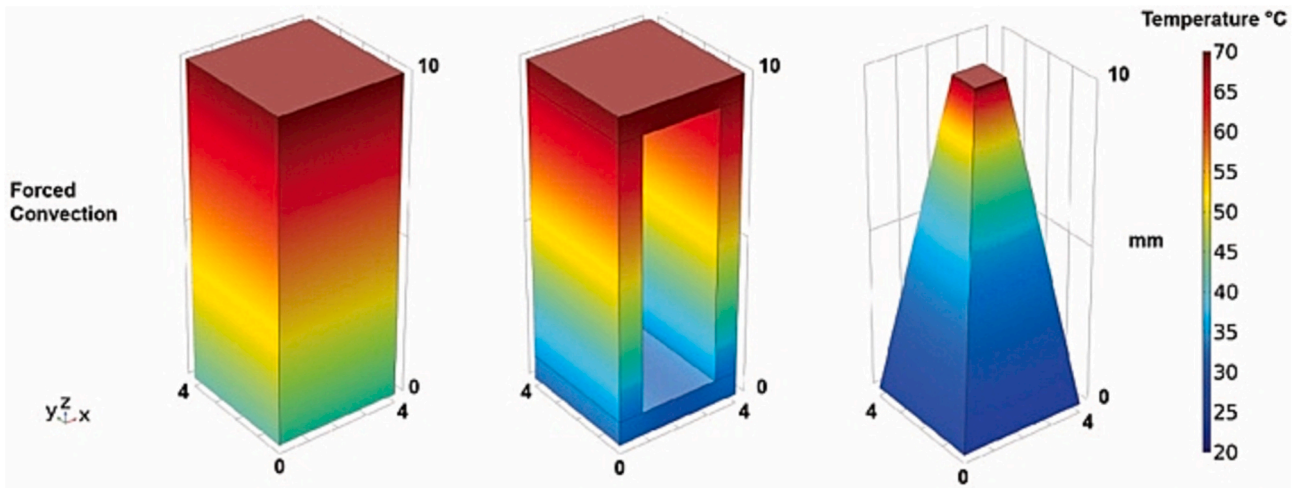


Fig. 2. Simulation results demonstrating the difference in the thermal gradient developed across three bismuth telluride geometries (from left to right): rectangular prism, hollow rectangle, and trapezoid. The simulations were performed with thermal boundary conditions of 70 °C on the hot side and forced convective cooling with a convection coefficient of $h = 200 \text{ W/m}^2\text{K}$ on the cold side [17].

2. Material and methods

2.1. Laser powder bed fusion (LPBF)

The LPBF system being employed for this study was a SLM125 from SLM Solutions Group AG (Lübeck, Germany).¹ It utilizes a single fiber laser from IPG Photonics (Oxford, Massachusetts) with adjustable power (0 W to 400 W) and scan speed (0 m/s to 10 m/s). The wavelength of the laser is 1070 nm, and the spot size is 60 μm . The chamber is kept under an inert argon environment during all builds, with the oxygen content held to <0.1 % (1000 ppm). For three-dimensional LPBF builds, four process parameters need to be defined: the laser power (p), laser scan-

ning speed (v), layer thickness (t), and hatch spacing (h) (Fig. 3).

2.2. Bismuth telluride powder synthesis

Mechanical milling techniques were employed to synthesize n-type bismuth telluride ($\text{Bi}_2\text{Te}_{2.7}\text{Se}_{0.3}$) alloy powder in an inert argon atmosphere. Constituent elements Bi (> 4 N purity, Alfa Aesar), Te (4 N purity, Alfa Aesar), and Se (5 N purity, Alfa Aesar) were weighed in appropriate quantities and loaded into a stainless steel (SS) vial. Several SS balls with diameters in the range of 10 mm to 12 mm were also added, and the vials were sealed in dry argon (99.999 % UHP). Depending on the quantity of starting materials, either high energy vibratory milling unit or planetary milling unit was employed. For smaller quantities (< 30 g), a SPEX 8000 Mixer/Mill high energy milling unit capable of vibrating at 1060 cycles/min. Was employed. For larger quantities (> 30 g), a Torrey Hills ND0.4 L planetary milling unit capable of rotating in both directions at 10 Hz (600 rpm) was used.

Milling was interrupted periodically for powder x-ray diffraction (XRD) of the milled powder to be conducted to assess the quality of the phase formation. Milling continued until only the XRD peaks for $\text{Bi}_2\text{Te}_{2.7}\text{Se}_{0.3}$ were observed. Typically, 11 h. to 16 h. of milling were required to obtain $\text{Bi}_2\text{Te}_{2.7}\text{Se}_{0.3}$ alloy without any observable impurities from XRD. Fig. 4 shows the final XRD spectrum collected for the planetary milled $\text{Bi}_2\text{Te}_{2.7}\text{Se}_{0.3}$ alloy powder with significant peaks indexed. Fig. 5 contains an SEM micrograph of the same planetary milled $\text{Bi}_2\text{Te}_{2.7}\text{Se}_{0.3}$ alloy powder, which possessed a range of sizes and irregular shapes.

For build substrates, p-type bismuth antimony telluride ingots were purchased from Tecteg Mfr. based in Ontario, Canada. These ingots were then sectioned using a diamond wafering blade into roughly 5 mm thick discs that could be used as substrates for the LPBF process.

2.3. Line scan experiments

To study the laser interaction with n-type bismuth telluride, line scan experiments were used. These line scans were run in the same SLM@125 system and across bulk n-type BiTeSe wafers from Coherent, an example of which is shown in Fig. 6a. Laser power (p) and scan speed (v) were adjusted as processing parameters for each line scan.

To measure the widths and depths of these melt pools, the laser-scanned discs with diameters of 2 cm (as in Fig. 6a) were polished to expose their cross-sections perpendicular to the laser scan direction. Then, these samples were etched in aqua regia (3 HCl: 1 HNO₃) for 15 s

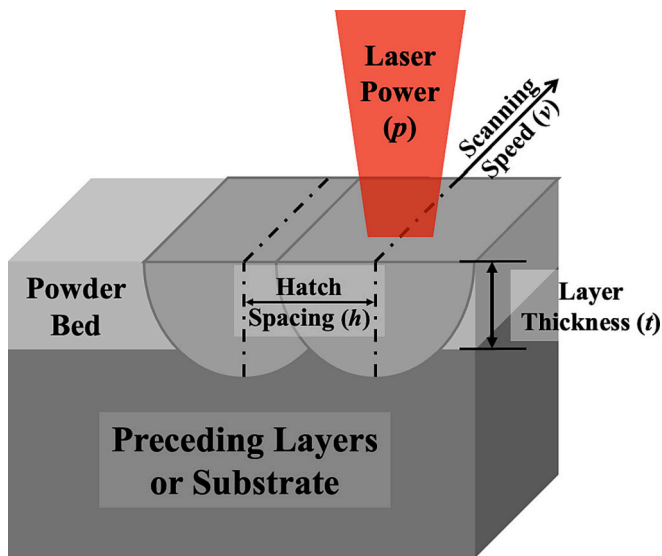


Fig. 3. LPBF process parameters: laser power (p), scanning speed (v), layer thickness (t), and hatch spacing (h).

¹ Certain commercial equipment instrumentation or materials are identified in this document. Such identification does neither imply recommendation or endorsement by the National Institute of Standards and Technology, nor it imply that the products identified are necessarily the best available for the purpose.

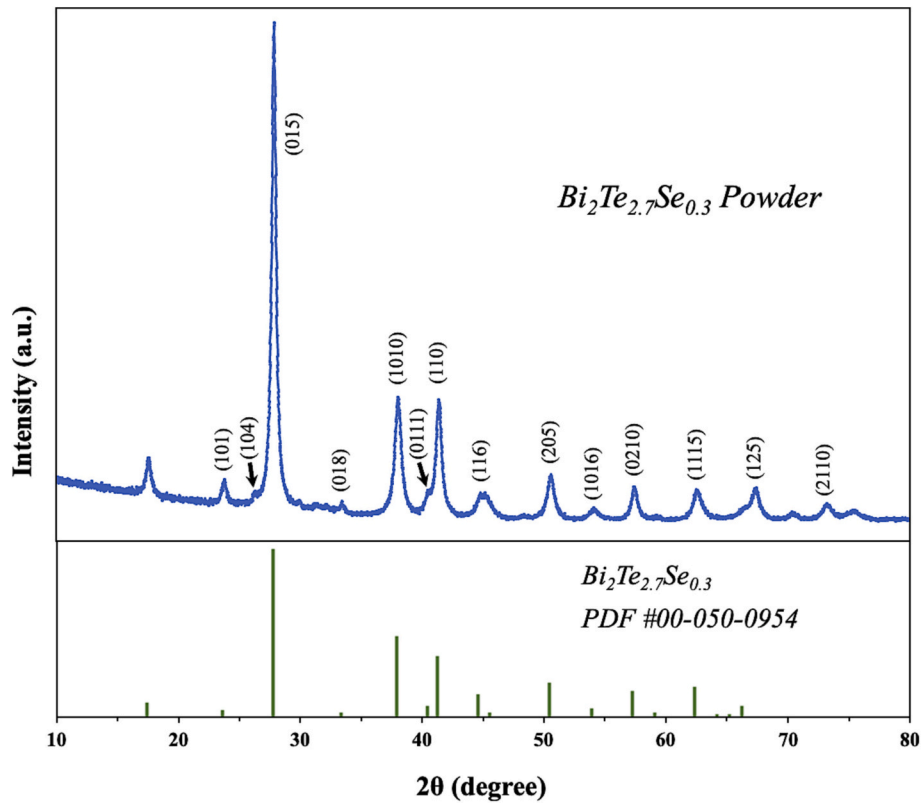


Fig. 4. XRD pattern of the planetary milled $\text{Bi}_2\text{Te}_{2.7}\text{Se}_{0.3}$ alloy powder. The spectrum is well-matched in position and intensities to the database values for $\text{Bi}_2\text{Te}_{2.7}\text{Se}_{0.3}$ (PDF#00-050-0954).

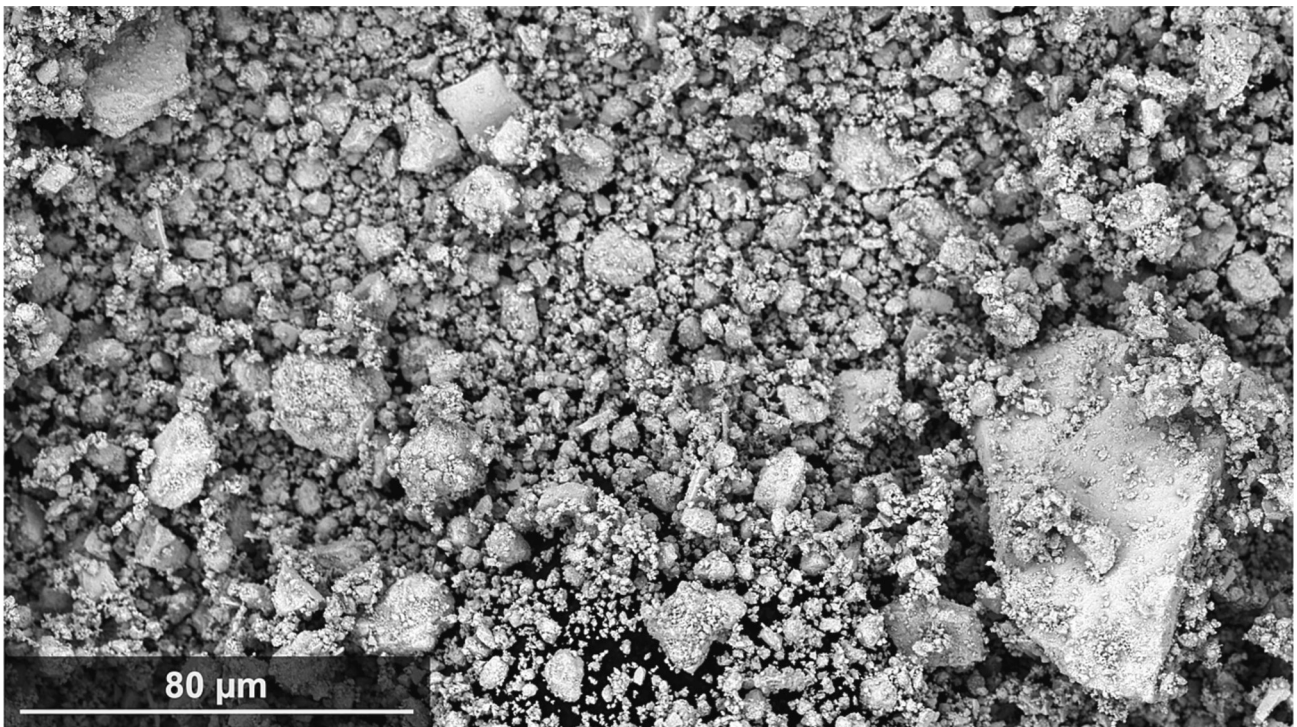


Fig. 5. Secondary electron micrograph of the planetary milled $\text{Bi}_2\text{Te}_{2.7}\text{Se}_{0.3}$ alloy powder.

to visualize the line scan melt pools. An example is shown in Fig. 6b. The melted region can be distinguished by the columnar grains bridging from the edges of the melt pools to their centers, in contrast to the

equiaxed grains of the surrounding unmelted material. Melt pool width and depth measurements were made from electron micrographs using ImageJ. We estimate the uncertainty for these measurements to be +/-

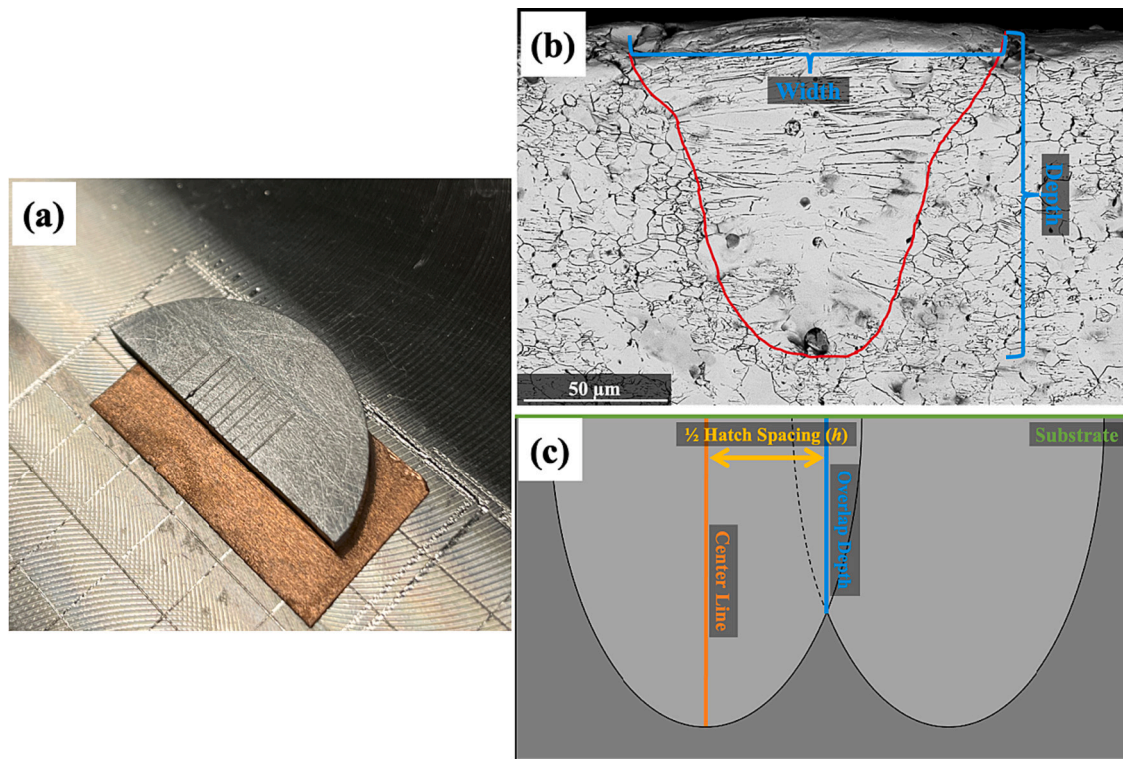


Fig. 6. (a) Multiple laser line scans run across a solid disc of n-type BiTeSe (diameter = 2 cm), shown adhered to the build plate using copper tape. (b) Backscattered electron micrograph of the cross-section (perpendicular to the laser scan direction) of a laser scan melt pool ($p = 20$ W, $v = 350$ mm/s) in n-type bismuth telluride that was etched for 15 s in aqua regia (3 HCl: 1 HNO₃). The melt pool is outlined in red. (c) Diagram demonstrating how to calculate the hatch spacing from a melt pool cross-section perpendicular to the laser scan direction. (For interpretation of the references to colour in this figure legend, the reader is referred to the web version of this article.)

5 %. This process was repeated across three cross-sections for each sample, so that multiple measurements could be averaged for each line scan and laser parameter combination (laser power and scan speed) to account for fluctuations in melt pool size along a single laser scan track [29,30].

These line scan melt pool tracks were used to determine the other two key parameters necessary for building three-dimensional parts in LPBF: hatch spacing (h) and layer thickness (t). The values for these parameters were chosen to ensure sufficient fusion between the adjacent line scans and consecutive layers of powder during the build. For this reason, the layer thickness was chosen first and could be no deeper than half the melt pool depth.

The process for determining the appropriate hatch spacing value is demonstrated using Fig. 6c. Adjacent line scans must overlap at a depth that is at least equivalent to the layer thickness. To account for the mild fluctuation in melt pool size along its track, an error of 25 % is assumed when deciding the overlap depth (i.e., overlap depth = $1.25 t$). This adjusted overlap depth is then found along the melt pool edges and a straight line is drawn up to the surface of the substrate. The distance between that overlap depth line and the center line of the melt pool is then measured and doubled to find the hatch spacing value. Another 20 % uncertainty is used when deciding the final hatch spacing value to account for the melt pool size fluctuations. This is a 20 % reduction in the measured hatch spacing value to bring the adjacent line scans closer together and increase their overlap (i.e., $h = 0.8 \times$ measured hatch spacing).

2.4. Three-dimensional sample fabrication and porosity measurements

Due to limitations in feedstock quantity and morphology, the LPBF builds were performed manually. The powder was deposited and leveled by hand in the argon-filled chamber of the SLM@125 system between

each layer. Powder spreading was accomplished through a rolling metal rod, which simulates the action of the recoater blade.

Rectangular bars of Bi₂Te_{2.7}Se_{0.3} were built with dimensions of 1.5 mm × 6 mm × 0.525 mm using a scan strategy where the scan tracks are parallel to the long axis of the samples without rotation between layers. To quantitatively evaluate their relative densities, the volume of the pores was estimated from micrographs and images such as those shown in Fig. 7. First, secondary electron micrographs were collected across multiple polished cross-sections perpendicular to the laser scans and long axis for each of the samples. Then, ImageJ was used to create a binary image that differentiated the pores from the polished surface based upon contrast. The porosity fraction was measured and averaged across three cross-sections for each sample.

When building the enhanced, nonstandard geometry parts, the same manual build strategy was employed, with powder deposition and leveling being carried out by hand in between layers in the SLM@125 build chamber. Additionally, the scan strategy was altered to minimize potential build defects. The line scan angles were rotated 33 degrees from layer to layer and were constrained to a 90 degree window centered around the shortest axis of the samples. This variation in direction and reduction in line scan vector length was used to reduce the buildup of thermal stress in the LPBF-built part [31,32].

2.5. Machine learning (ML)

The goal of ML is to predict melt pool width and depth as a function of LPBF process parameters (laser power and scan speed). In addition, the trained models should be able to quantify uncertainties in the predicted values. We accomplished the task by building an ensemble of ML models (as opposed to a single ML model) using the bootstrap resampling method, which is a well-known sampling technique used to estimate statistics on a population by sampling the dataset with replacement

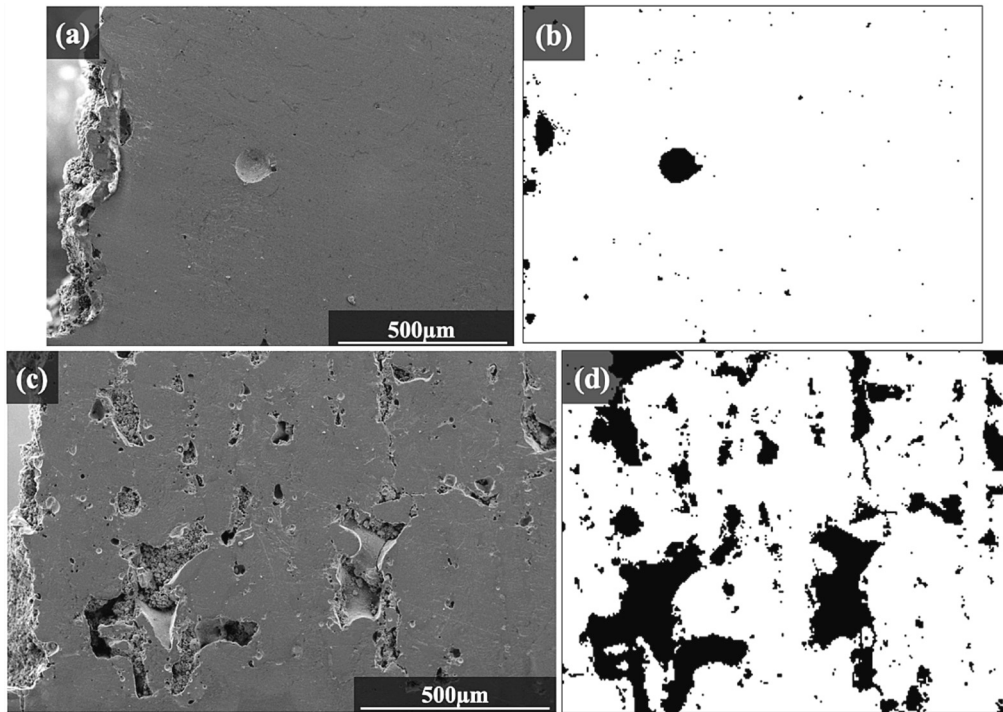


Fig. 7. Representative porosity calculations for LPBF-built $\text{Bi}_2\text{Te}_{2.7}\text{Se}_{0.3}$ parts demonstrating low porosity (a & b: $p = 25$ W, $v = 100$ mm/s, $h = 90$ μm , $t = 75$ μm) and high porosity (c & d: $p = 25$ W, $v = 400$ mm/s, $h = 130$ μm , $t = 75$ μm). (a, c) show the secondary electron micrographs and (b, d) show the binary images created through ImageJ that mark all pores in black.

(i.e., the bootstrapped dataset can have multiple duplicate entries) [33]. For example, if we considered 50 bootstrap samples, then we trained 50 independent ML models. The mean value and standard deviation from the 50 trained models are then used as the predicted response and the associated uncertainty in the response, respectively. Hence the name ensemble ML, which is a well-established approach in the materials informatics literature [34–37].

Support vector regression (SVR) was employed as the ML method for ensemble model building [34,38]. In general, SVR is of the form,

$$f(\mathbf{x}) = \langle \mathbf{w}, \mathbf{x} \rangle + \mathbf{b}, \quad (1)$$

where \mathbf{x} is a vector of descriptors, \mathbf{w} are coefficients that fit the training data, and \mathbf{b} is the intercept. The objective function is then given in Eq. (2):

$$\min_{\frac{1}{2} \|\mathbf{w}\|^2 + C \sum_{i=1}^n (\xi_i + \xi_i^*)} \quad (2)$$

$$\text{subject to } \begin{cases} f(\mathbf{x}) - \langle \mathbf{w}, \mathbf{x}_i \rangle - \mathbf{b} \leq \epsilon + \xi_i \\ \langle \mathbf{w}, \mathbf{x}_i \rangle + \mathbf{b} - f(\mathbf{x}) \leq \epsilon + \xi_i^* \\ \xi_i, \xi_i^* \geq 0 \end{cases}, \text{ where } C \text{ is the regularization}$$

term, n is the total number of data points, ϵ is the insensitive tube around the target values that provides the magnitude of the amount of permitted error (only those target values greater than ϵ are penalized by the optimization), ξ_i, ξ_i^* are the nonnegative slack variables that permit a certain level of violation of the ϵ -tube bounds, and \mathbf{x}_i is the descriptor for the i^{th} training data. The regularization term C balances the model complexity and training error (large C and small C can lead to overfitting and underfitting, respectively). In this work, we use the nonlinear Gaussian radial basis function of the form:

$$\kappa(\mathbf{x}, \mathbf{x}') = \exp\left(-\frac{\|\mathbf{x} - \mathbf{x}'\|^2}{2\sigma^2}\right). \quad (3)$$

The hyperparameters, C and σ were determined by using leave-one-out cross-validation (LOOCV) from the training data to balance the bias–variance tradeoff. We chose four different values for the number of bootstrap samples: {25, 50, 75, 100}. The following values were explored for $C = \{0.001, 0.01, 0.1, 1, 2, 3, 4, 5, 6, 7, 8, 9, 10, 100\}$ and $\sigma = \{0.001, 0.01, 0.1, 0.2, 0.3, 0.4, 0.5, 0.6, 0.7, 0.8, 0.9, 1.0\}$. For each bootstrap resample dataset, exhaustive grid search was used for hyperparameter optimization. Finally, the hyperparameters that minimize the LOOCV error are used for training the final model. The SVR method was utilized as implemented in the open source e1071 R-package for this work [39]. After model training, the mean and standard deviation were calculated from the ensemble of SVR models and served as the ML prediction of melt pool width (or depth) and the associated uncertainties, respectively.

3. Results and discussion: Laser-material interactions

3.1. Melt Pool width and depth maps

The initial step of process optimization was an iterative combination of ML and experimental data that produced predictive models for the melt pool widths and depths within the build parameter space of interest. The iterative augmented learning strategy is schematically shown in Fig. 8.

First, a small experimental dataset was generated to create an initial model using ML. Multiple laser lines were scanned across a solid substrate of n-type bismuth telluride, an example of which is shown in Fig. 6a. In total, 13 line scans were conducted with laser powers (p) ranging from 10 W to 40 W and laser scan speeds (v) ranging from 250 mm/s to 550 mm/s. These values spanned the initial parameter space of interest, which was chosen to expand around the parameter combinations that had previously been tested in similar works [10,12,19,21]. The melt pool widths and depths for these initial line scan parameter combination experiments were measured experimentally as in Fig. 6b and can be found in Table 1.

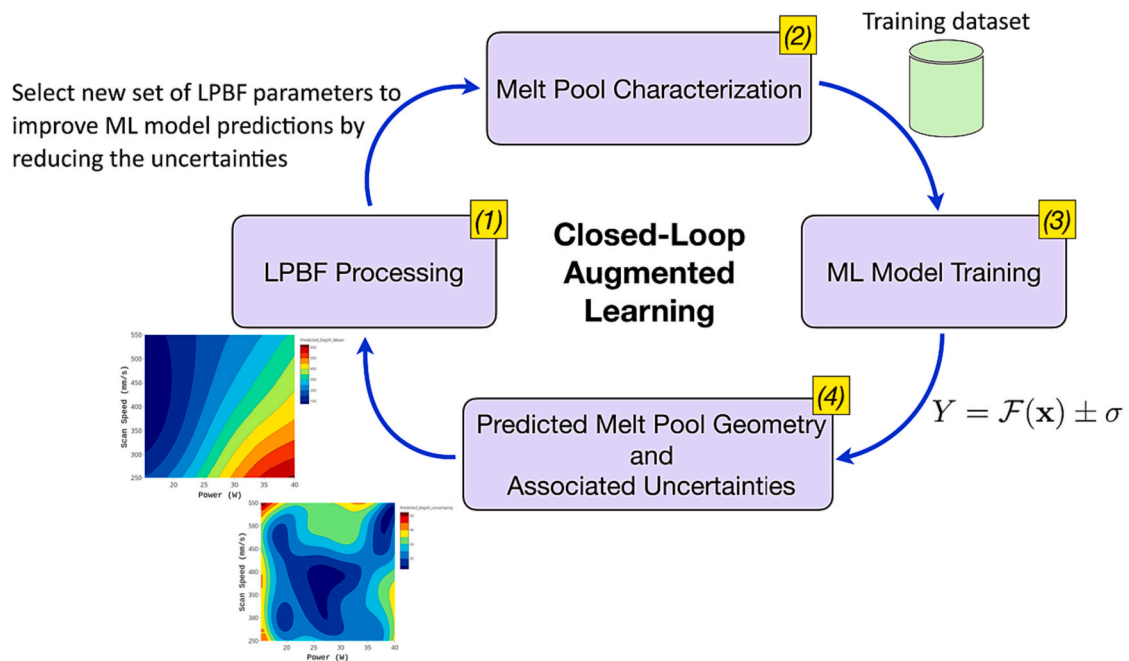


Fig. 8. A schematic showing the iterative augmented learning strategy used to develop a predictive understanding of the melt pool geometry (width and depth) using LPBF processing of n-type Bi₂Te_{2.7}Se_{0.3} thermoelectric. A total of six iterations were performed with feedback.

Table 1

Initial experimental and ML-predicted line scan data used to generate the predicted melting behavior maps from ML. We estimate the uncertainty for the experimentally measured dimensions to be $\pm 5\%$ (1 sigma). Italicized parameter combinations were ultimately chosen to build three-dimensional, rectangular bar samples. These 13 line scan parameter combinations represent the first iteration of experimental data used to train the initial ML model. Ultimately, 93 line scan parameter combinations were used to generate the final ML predictive model for n-type bismuth telluride melt pool dimensions.

Line Scan Parameters		Experimental Dimensions		ML-Predicted Dimensions		ML Prediction Uncertainty		Relative Uncertainty	
Power p (W)	Scan Speed v (mm/s)	Width (μm)	Depth (μm)	Width (μm)	Depth (μm)	Width (μm)	Depth (μm)	Width	Depth
10	300	No melting		No melting		No melting		No melting	
10	400	No melting		No melting		No melting		No melting	
10	550	No melting		No melting		No melting		No melting	
<i>20</i>	<i>350</i>	<i>125</i>	<i>117</i>	<i>128</i>	<i>130</i>	<i>13.5</i>	<i>20.7</i>	<i>0.105</i>	<i>0.159</i>
<i>20</i>	<i>450</i>	<i>110</i>	<i>86.5</i>	<i>118</i>	<i>104</i>	<i>12.0</i>	<i>19.3</i>	<i>0.101</i>	<i>0.186</i>
20	550	99.0	75.0	112	112	12.4	34.9	0.111	0.312
25	350	133	237	149	235	13.1	14.8	0.088	0.063
25	350	136	239	149	235	13.1	14.8	0.088	0.063
25	400	135	207	150	201	9.08	13.4	0.061	0.067
25	400	128	215	150	201	9.08	13.4	0.061	0.067
30	300	151	412	187	405	19.6	19.5	0.105	0.048
30	500	124	267	165	228	24.6	33.3	0.149	0.146
40	250	172	626	200	607	42.0	37.7	0.211	0.062

The absence of a melt pool indicated that no melting occurred for that line scan parameter combination. It was observed experimentally and predicted using ML that no melting occurs when the laser power is below 15 W. Therefore, the parameter space could be narrowed to exclude this nonmelting region going forward.

The ten experimentally measured melt pool dimensions were then used to create the initial model from ML, which was visualized using a heat map. An additional heat map was also created that showed the uncertainty of the model's predictions within the same parameter space. Subsequent line scan experiments were chosen that targeted parameter combinations in the regions with greater uncertainties. In total, 93 line scan parameter combinations were conducted and their melt pools measured across six iterations of closed-loop augmented learning with feedback. Ultimately, the final melt pool width and depth ML prediction maps were generated from these 93 data points and are shown in Fig. 9. The associated uncertainty maps are also provided in Fig. 10. The ML-predicted melt pool dimensions and associated uncertainties can be found in Table 1 for the initial 13 line scan parameter combinations.

Several trends were observed from these melt pool dimension prediction maps. First, as the input energy density (IED) is increased by either increasing the laser power (p) or decreasing the laser scanning speed (v), the melt pool dimensions become larger. This matches expectations well for laser-based AM processes [20,40–42]. Additionally, for the melt pool depth prediction map shown in Fig. 9b, the contour lines become shallower and more horizontal for higher IED processing parameters (high p , low v), so the laser scanning speed (v) has a greater impact on the melt pool depth in this region. In contrast, the slope increases and becomes more vertical in the lower IED processing region (low p , high v), which indicates the laser power (p) has a greater impact on the melt pool depth for these laser parameters.

For the melt pool width prediction map shown in Fig. 9a, trends in the slope are less clear. However, as the laser power and scanning speed both increase (upper right corner), the growth in melt pool width diminishes until a region is reached where the change in melt pool width is less pronounced despite variations in the laser parameters. Once again, evidence of these stagnant melt pool widths at high laser powers and

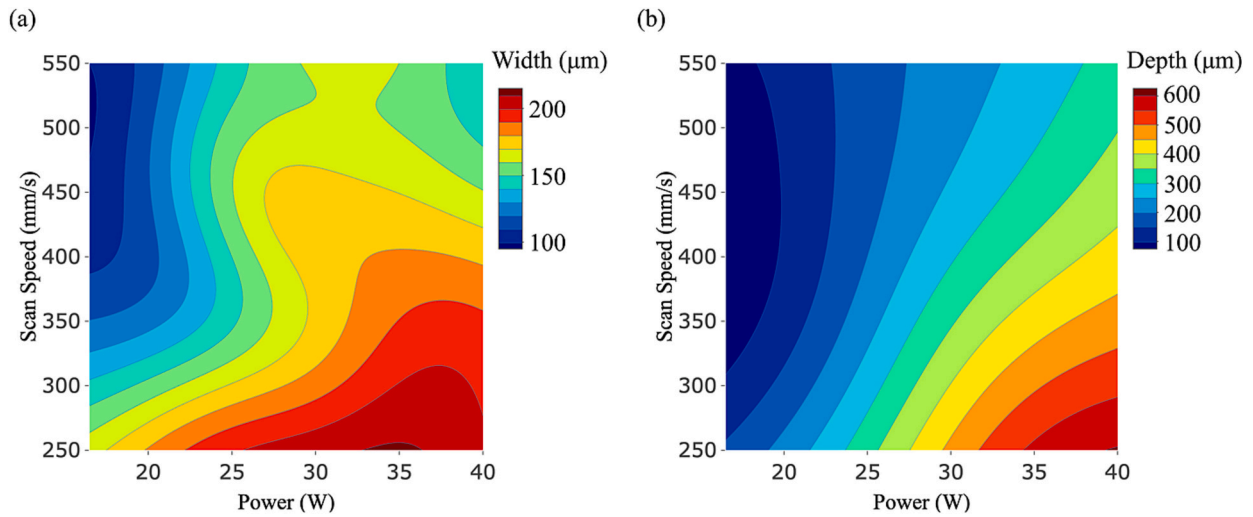


Fig. 9. ML-predicted melt pool (a) width and (b) depth maps for n-type bismuth telluride ($\text{Bi}_2\text{Te}_{2.7}\text{Se}_{0.3}$).

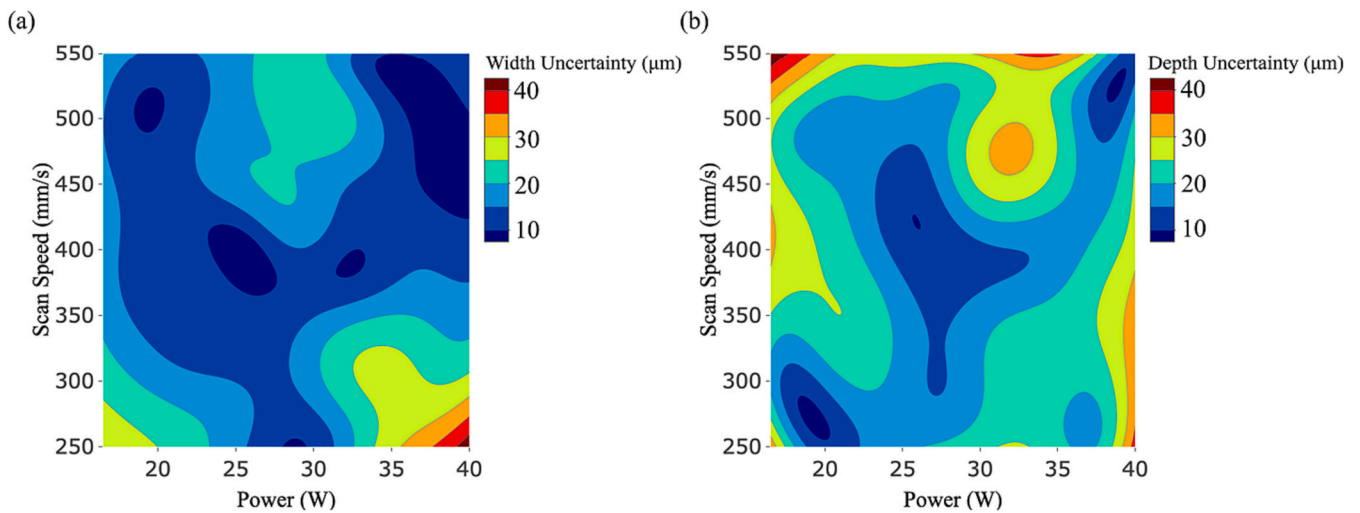


Fig. 10. Uncertainties in ML-predicted melt pool (a) width and (b) depth maps for n-type bismuth telluride ($\text{Bi}_2\text{Te}_{2.7}\text{Se}_{0.3}$).

scanning speeds has been observed in literature [20,43]. The observation of these trends is valuable when attempting to tune the desired shape of the melt pool by preferentially adjusting the laser power or scan speed to intentionally manipulate the melt pool dimensions.

The uncertainty values shown in Fig. 10 have multiple contributing factors, including sampling, model, and experimental errors. It is common to classify uncertainties from ML into two types: Type A (*aleatoric* or statistical) and Type B (*epistemic* or systematic) [44,45]. While the Type A uncertainty can be reduced by sampling data points in the LPBF processing space where the ML model is ignorant, it is not straightforward to reduce the contribution from the aleatoric uncertainty. In this work, one of the key contributors to these uncertainties were experimental sample-to-sample variations.

The presence of defects (*e.g.*, pores, cracks) was also recorded for various laser parameter combinations. Pore frequency and volume tended to be greater for line scans run using higher IED values. This is consistent with well-established knowledge in LPBF: higher energy density line scans tend to cause keyholing and the formation of vapor depression zones that leave behind gas pores when solidified [20,46]. Cracking was not observed in the line scan melt pools.

4. AM of three-dimensional builds

4.1. Determination of build parameters

Following single track laser scans and characterization of melt pool geometries, it is possible to use the predictive maps shown in Fig. 9 to determine the parameter combinations that could minimize defect concentration in three-dimensional parts of n-type bismuth telluride ($\text{Bi}_2\text{Te}_{2.7}\text{Se}_{0.3}$). For these bulk builds, the four process parameters that need to be defined are the laser power (p), scanning speed (v), layer thickness (t), and hatch spacing (h) (Fig. 3).

Using the melt pool width and depth prediction maps (Fig. 9), parameter combinations were chosen that yielded melt pools with a low uncertainty in melt pool geometries and a moderate depth to width ratio to minimize potential porosity. Larger uncertainties in the final ML predictions were assumed to be indicative of an increased inconsistency in the melt pool sizes. Relative uncertainty values, shown in Table 1, were calculated by dividing the ML prediction uncertainties in width or depth by their associated width or depth predicted values, respectively. A maximum relative uncertainty of 0.2 was established to ensure consistency between the laser scans of the LPBF build.

Within laser-based AM, when the melt pool depth to width ratio is large, keyhole porosity is often generated due to the instability of the

vapor depression region [20,47]. A maximum depth to width ratio of 1.5 was established for this study. On the other hand, shallow melt pools can increase the risk for lack of fusion porosity due to incomplete melting. Optimized laser parameter combinations are chosen to generate melt pools between these two extremes and in a defect-free regime to build highly dense parts [48]. A diagram of a generic AM processing map containing these three processing regimes can be found in Fig. 11.

Following this process, the final build parameter combinations were determined: 1) $p = 20$ W, $v = 350$ mm/s, $h = 56$ μ m; 2) $p = 25$ W, $v = 400$ mm/s, $h = 40$ μ m; 3) $p = 20$ W, $v = 450$ mm/s, $h = 48$ μ m; and 4) $p = 20$ W, $v = 350$ mm/s, $h = 70$ μ m. A layer thickness (t) of 35 μ m was used when building all four samples. Sample 4 uses the same laser parameters as sample 1, except with a larger hatch distance. These chosen laser parameter combinations and associated melt pool width and depth information are italicized in Table 1.

4.2. Sample fabrication and characterization

$\text{Bi}_2\text{Te}_{2.7}\text{Se}_{0.3}$ rectangular bars were then fabricated, and representative scanning electron microscopy (SEM) micrographs of their cross-sections are shown in Fig. 12. While a few cracks were observed in the substrate, no cracks were present in samples 1–3. In contrast, sample 4 did show signs of cracking, particularly near its top surface.

Three cross-sectional images for each sample were used to measure the average sample porosities using the process shown in Fig. 7. Ultimately, it was found that the average porosities (\pm standard deviation) of these samples were 1: 1.4 % (\pm 0.5 %), 2: 0.9 % (\pm 0.9 %), 3: 3.8 % (\pm 0.4 %), and 4: 8.2 % (\pm 1.3 %). To our knowledge, this is the lowest porosity and highest relative density that has been reported through the LPBF AM of bismuth telluride. Since bismuth telluride is a brittle and often difficult to process material with no room temperature ductility [49], successful fabrication of crack-free and highly dense samples demonstrates the ability of this newly developed protocol to find process parameters that can successfully build high quality parts out of a new AM material.

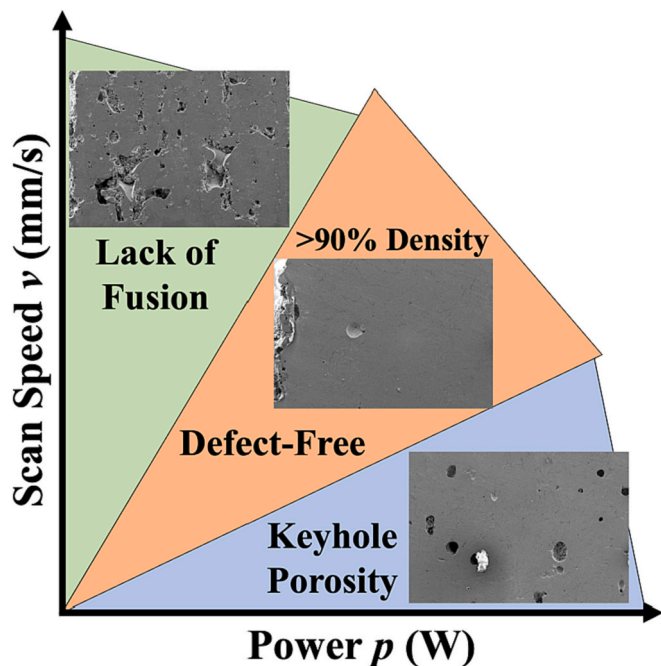


Fig. 11. General AM processing map that demonstrates the three distinct processing regimes: lack of fusion, defect-free, and keyholing mode zones.

5. Fabrication of enhanced geometry parts

5.1. Additively Manufactured thermoelectric parts with nonstandard geometries

In order to test the predictive capabilities of this augmented ML process, we utilized it to search for optimized parameters for a significantly larger layer thickness (t). The initial builds shown in Fig. 12 were conducted with a layer thickness of 35 μ m, which is in the lower range of parameters commonly used by both researchers and industry. Building with larger layer thicknesses is typically preferable to reduce the total build time, but it is often challenging due to large melt pool size requirements and increased risk for lack of fusion or keyhole porosity. Here, we choose a layer thickness of $t = 75$ μ m, which would reduce building time by >50 % when compared to a 35 μ m layer thickness.

Based upon the results of bar sample 2 (Fig. 12), the laser parameter combination of $p = 25$ W and $v = 400$ mm/s was selected for creating $\text{Bi}_2\text{Te}_{2.7}\text{Se}_{0.3}$ parts with enhanced, nonstandard geometries. This was because bar sample 2 was both entirely devoid of cracks and had a very low porosity fraction of 0.9 % (\pm 0.9 %). Additionally, ML predicted that the melt pool depth for $p = 25$ W and $v = 400$ mm/s was 201 μ m (Table 1), which meant that this laser parameter combination would be an acceptable choice at over double the depth of this new layer thickness. Following the method discussed in Section 2.3 and shown in Fig. 6c, the new hatch spacing was calculated to be 80 μ m. The final processing parameters were selected as: $p = 25$ W, $v = 400$ mm/s, $h = 80$ μ m, and $t = 75$ μ m.

The LPBF-built complex geometries were chosen based on the prior modeling work (shown in Fig. 2) that predicted these geometries could increase the TE efficiency of $\text{Bi}_2\text{Te}_{2.7}\text{Se}_{0.3}$ parts [17,18]. These three geometries were the rectangular prism, hollow rectangle, and trapezoid. The rectangular prism was chosen as a control sample with dimensions of 4 mm \times 4 mm \times 10 mm, comparable to traditionally manufactured TE legs. The hollow rectangle also had outer dimensions of 4 mm \times 4 mm \times 10 mm, with a wall thickness of 0.75 mm. The trapezoid had a length of 10 mm, a 4 mm \times 4 mm large base, and a 1 mm \times 1 mm small face.

Using the new processing parameters and scan strategy, $\text{Bi}_2\text{Te}_{2.7}\text{Se}_{0.3}$ parts were successfully constructed in the rectangular prism, hollow rectangle, and trapezoid geometries (Fig. 13). The parts show no visible cracks and are mechanically sound after removal from the substrate. Further, these parts were measured to have a relative density of 98.6 % (\pm 1 %) using the Archimedes method. The incorporation of ML modeling removed the need for additional experiments and allowed for the selection of new processing parameters for an increased layer thickness to successfully build high quality parts faster.

6. Conclusions

An iterative system of ML predictive modeling and experimental validation was designed and allowed for the rapid discovery of LPBF processing parameters capable of building highly dense, crack-free $\text{Bi}_2\text{Te}_{2.7}\text{Se}_{0.3}$ parts with enhanced geometries. Through this iterative process, prediction maps of the entire processing parameter space were quickly and efficiently derived for n-type bismuth telluride ($\text{Bi}_2\text{Te}_{2.7}\text{Se}_{0.3}$).

The integration of ML techniques meant that a visualization and understanding of changing melt pool dimensions in response to varied laser parameters were quickly achieved. Optimized parameter combinations were then intentionally chosen and used to LPBF complex $\text{Bi}_2\text{Te}_{2.7}\text{Se}_{0.3}$ parts with a high build quality. The existing prediction model could also be used rapidly identify processing parameters for larger layer thicknesses and faster builds without additional experimental effort. These results are not only significant to the field of TE, but this new augmented ML approach can be more broadly applied when developing a processing strategy for any new AM material.

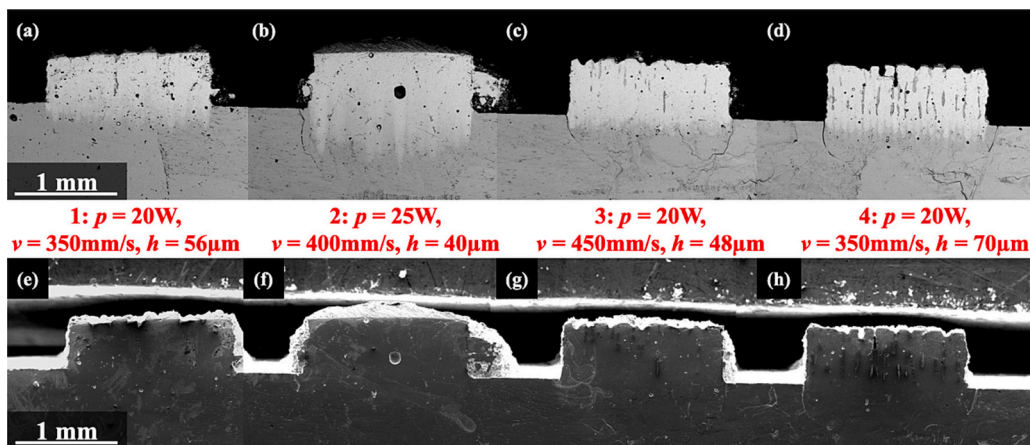


Fig. 12. Representative SEM micrographs of the cross-sections of LPBF-built $\text{Bi}_2\text{Te}_{2.7}\text{Se}_{0.3}$ parts. Backscattered electron micrographs shown on top (a, b, c, & d) and secondary electron micrographs shown on bottom (e, f, g, & h). Build parameter combinations used are: (1: a & e) $p = 20$ W, $v = 350$ mm/s, $h = 56$ μm ; (2: b & f) $p = 25$ W, $v = 400$ mm/s, $h = 40$ μm ; (3: c & g) $p = 20$ W, $v = 450$ mm/s, $h = 48$ μm ; and (4: d & h) $p = 20$ W, $v = 350$ mm/s, $h = 70$ μm . A layer thickness (t) of 35 μm was used when building all four samples.



Fig. 13. LPBF-built $\text{Bi}_2\text{Te}_{2.7}\text{Se}_{0.3}$ parts with nonstandard geometries. Prior to part removal, the substrate was mounted in a polymer epoxy to prevent cracks within the substrate from propagating into and breaking the $\text{Bi}_2\text{Te}_{2.7}\text{Se}_{0.3}$ parts.

Declaration of competing interest

The authors declare that they have no known competing financial interest or personal relationships that could have appeared to influence the work reported in this paper.

Acknowledgements

This work was partially supported by the Department of Energy (DOE Award #DE-EE0009100). R.J.H. acknowledges funding support from the Virginia-North Carolina Louis Stokes Alliance for Minority Participation Bridge to the Doctorate Fellowship.

References

- [1] He J, Tritt TM. Advances in thermoelectric materials research: looking back and moving forward. *Science* 2017;357. <https://doi.org/10.1126/science.aak9997>.
- [2] Tan G, Zhao LD, Kanatzidis MG. Rationally designing high-performance bulk thermoelectric materials. *Chem. Rev.* 2016;116:12123–49. <https://doi.org/10.1021/acs.chemrev.6b00255>.
- [3] Forman C, Muritala IK, Pardemann R, Meyer B. Estimating the global waste heat potential. *Renew. Sust. Energ. Rev.* 2016;57:1568–79. <https://doi.org/10.1016/j.rser.2015.12.192>.
- [4] Snyder GJ, LeBlanc S, Crane D, Pangborn H, Forest CE, Rattner A, et al. Distributed and localized cooling with thermoelectrics. *Joule* 2021;5:748–51. doi:<https://doi.org/10.1016/j.joule.2021.02.011>.
- [5] Chen ZG, Hana G, Yanga L, Cheng L, Zou J. Nanostructured thermoelectric materials: current research and future challenge. *Prog Nat Sci Mater Int* 2012;22: 535–49. <https://doi.org/10.1016/j.pnsc.2012.11.011>.
- [6] Bohorquez WOI, Barbosa JR, Nogueira LAH, Lora EES. Repowering: An option for refurbishment of old thermal power plants in Latin-American countries. In: *Proc ASME Turbo Expo*, 1; 2010. p. 825–34. <https://doi.org/10.1115/GT2010-23058>.
- [7] El-Desouky A, Carter M, Andre MA, Bardet PM, LeBlanc S. Rapid processing and assembly of semiconductor thermoelectric materials for energy conversion devices. *Mater. Lett.* 2016;185:598–602. <https://doi.org/10.1016/j.matlet.2016.07.152>.
- [8] He R, Schierning G, Nielsch K. Thermoelectric devices: a review of devices, architectures, and contact optimization. *Adv. Mater. Technol.* 2018;3. <https://doi.org/10.1002/admt.201700256>.
- [9] Oztan C, Welch R, Leblanc S. Additive manufacturing of bulk thermoelectric architectures: a review. *Energies* 2022;15. <https://doi.org/10.3390/en15093121>.
- [10] El-Desouky A, Carter M, Mahmoudi M, Elwany A, LeBlanc S. Influences of energy density on microstructure and consolidation of selective laser melted bismuth telluride thermoelectric powder. *J. Manuf. Process.* 2017;25:411–7. <https://doi.org/10.1016/j.jmapro.2016.12.008>.
- [11] Zheng Y, Slade TJ, Hu L, Tan XY, Luo Y, Luo Z-Z, et al. Defect engineering in thermoelectric materials: what have we learned? *Chem. Soc. Rev.* 2021;50: 9022–54. <https://doi.org/10.1039/d1cs00347j>.
- [12] Mao Y, Yan Y, Wu K, Xie H, Xiu Z, Yang J, et al. Non-equilibrium synthesis and characterization of n-type $\text{Bi}_2\text{Te}_{2.7}\text{Se}_{0.3}$ thermoelectric material prepared by rapid laser melting and solidification. *RSC Adv.* 2017;7:21439–45. <https://doi.org/10.1039/c7ra02677c>.
- [13] Zhang Q, Gu B, Wu Y, Zhu T, Fang T, Yang Y, et al. Evolution of the intrinsic point defects in bismuth telluride-based thermoelectric materials. *ACS Appl. Mater. Interfaces* 2019;11:41424–31. <https://doi.org/10.1021/acsami.9b15198>.
- [14] Zhu TJ, Hu LP, Zhao XB, He J. New insights into intrinsic point defects in v2vi3 thermoelectric materials. *Adv. Sci.* 2016;3. <https://doi.org/10.1002/advs.201600004>.
- [15] Hu L, Zhu T, Liu X, Zhao X. Point defect engineering of high-performance bismuth-telluride-based thermoelectric materials. *Adv. Funct. Mater.* 2014;24:5211–8. <https://doi.org/10.1002/adfm.201400474>.
- [16] Horn TJ, Harrysson OLA. Overview of current additive manufacturing technologies and selected applications. *Sci. Prog.* 2012;95:255–82. <https://doi.org/10.3184/003685012X13420984463047>.
- [17] Şişik B, LeBlanc S. The influence of leg shape on thermoelectric performance under constant temperature and heat flux boundary conditions. *Front Mater* 2020;7:1–13. <https://doi.org/10.3389/fmats.2020.595955>.
- [18] Thimont Y, Leblanc S. The impact of thermoelectric leg geometries on thermal resistance and power output. *J. Appl. Phys.* 2019;126. <https://doi.org/10.1063/1.5115044>.

- [19] Zhang H, Hobbs D, Nolas GS, Leblanc S. Laser additive manufacturing of powdered bismuth telluride. *J. Mater. Res.* 2018;33:4031–9. <https://doi.org/10.1557/jmr.2018.390>.
- [20] Guo Q, Zhao C, Qu M, Xiong L, Escano LI, Hojjatzadeh SMH, et al. In-situ characterization and quantification of melt pool variation under constant input energy density in laser powder bed fusion additive manufacturing process. *Addit. Manuf.* 2019;28:600–9. <https://doi.org/10.1016/j.addma.2019.04.021>.
- [21] Wu K, Yan Y, Zhang J, Mao Y, Xie H, Yang J, et al. Preparation of n-type Bi₂Te₃ thermoelectric materials by non-contact dispenser printing combined with selective laser melting. In: *Phys Status Solidi - Rapid Res Lett*, 11; 2017. <https://doi.org/10.1002/pssr.201700067>.
- [22] Mondal S, Gwynn D, Ray A, Basak A. Investigation of melt pool geometry control in additive manufacturing using hybrid modeling. In: *Metals (Basel)*, 10; 2020. p. 1–23. <https://doi.org/10.3390/met10050683>.
- [23] Seede R, Shoukr D, Zhang B, Whitt A, Gibbons S, Flater P, et al. An ultra-high strength martensitic steel fabricated using selective laser melting additive manufacturing: densification, microstructure, and mechanical properties. *Acta Mater.* 2020;186:199–214. <https://doi.org/10.1016/j.actamat.2019.12.037>.
- [24] Kusano M, Kitano H, Watanabe M. Novel calibration strategy for validation of finite element thermal analysis of selective laser melting process using Bayesian optimization. In: *Materials (Basel)*, 14; 2021. <https://doi.org/10.3390/ma14174948>.
- [25] Wang Z, Jiang C, Liu P, Yang W, Zhao Y, Horstemeyer MF, et al. Uncertainty quantification and reduction in metal additive manufacturing. *Npj Comput Mater* 2020;6. <https://doi.org/10.1038/s41524-020-00444-x>.
- [26] Ye J, Yasin MS, Muhammad M, Liu J, Vinel A, Silva D, et al. Bayesian Process Optimization for Additively Manufactured Nitinol. *Solid Free. Fabr. 2021 Proc. 32nd Annu. Int.*, 2021, p. 284–96.
- [27] Kitano H, Kusano M, Tsujii M, Yumoto A, Watanabe M. Process parameter optimization framework for the selective laser melting of hastelloy x alloy considering defects and solidification crack occurrence. *Crystals* 2021;11. <https://doi.org/10.3390/cryst11060578>.
- [28] Agarwal A, Banerjee T, Gockel J, LeBlanc S, Walker J, Middendorf J. Predicting Thermoelectric Power Factor of Bismuth Telluride During Laser Powder Bed Fusion Additive Manufacturing. *ArXiv E-Prints* 2023:arXiv:2303.15663. doi:10.48550/arXiv.2303.15663.
- [29] Gould B, Wolff S, Parab N, Zhao C, Lorenzo-Martin MC, Fezzaa K, et al. In situ analysis of laser powder bed fusion using simultaneous high-speed infrared and X-ray imaging. *Jom* 2021;73:201–11. <https://doi.org/10.1007/s11837-020-04291-5>.
- [30] Parab ND, Zhao C, Cunningham R, Escano LI, Fezzaa K, Everhart W, et al. Ultrafast X-ray imaging of laser–metal additive manufacturing processes. *J. Synchrotron Radiat.* 2018;25:1467–77. <https://doi.org/10.1107/S1600577518009554>.
- [31] Kruth JP, Deckers J, Yasa E, Wauthlé R. Assessing and comparing influencing factors of residual stresses in selective laser melting using a novel analysis method. *Proc Inst Mech Eng Part B J Eng Manuf* 2012;226:980–91. <https://doi.org/10.1177/0954405412437085>.
- [32] Ali H, Ghadbeigi H, Mumtaz K. Effect of scanning strategies on residual stress and mechanical properties of selective laser melted Ti6Al4V. *Mater. Sci. Eng. A* 2018; 712:175–87. <https://doi.org/10.1016/j.msea.2017.11.103>.
- [33] Efron B. In: Kotz S, Johnson NL, editors. *Bootstrap methods: Another look at the jackknife BT - breakthroughs in statistics: Methodology and distribution*. New York, NY: Springer New York; 1992. p. 569–93. https://doi.org/10.1007/978-1-4612-4380-9_41.
- [34] Balachandran PV. Adaptive machine learning for efficient materials design. *MRS Bull.* 2020;45:579–86. <https://doi.org/10.1557/mrs.2020.163>.
- [35] Morgan D, Jacobs R. Opportunities and challenges for machine learning in materials science. *Annu. Rev. Mater. Res.* 2020;50:71–103. <https://doi.org/10.1146/annurev-matsci-070218-010015>.
- [36] Huelsenbeck L, Jung S, Herrera Del Valle R, Balachandran PV, Giri G. Accelerated HKUST-1 thin-film property Optimization using active learning. *ACS Appl. Mater. Interfaces* 2021;13:61827–37. <https://doi.org/10.1021/acsami.1c20788>.
- [37] Nawa K, Hagiwara K, Nakamura K. Prediction-accuracy improvement of neural network to ferromagnetic multilayers by Gaussian data augmentation and ensemble learning. *Comput. Mater. Sci.* 2023;219:112032. <https://doi.org/10.1016/j.commatsci.2023.112032>.
- [38] Smola AJ, Schölkopf B. A tutorial on support vector regression. *Stat. Comput.* 2004;14:199–222. <https://doi.org/10.1023/B:STCO.0000035301.49549.88>.
- [39] Karatzoglou A, Meyer D, Hornik K. Support vector algorithm in R. *J. Stat. Softw.* 2006;15:1–28.
- [40] Wang T, Wang Y, Chen C, Zhu H. Relationships between the characteristics of porosity, melt pool and process parameters in laser powder bed fusion Al Zn alloy. *J. Manuf. Process.* 2021;68:1236–44. <https://doi.org/10.1016/j.jmapro.2021.06.027>.
- [41] Kusuma C, Ahmed SH, Mian A, Srinivasan R. Effect of laser power and scan speed on melt Pool characteristics of commercially pure titanium (CP-Ti). *J. Mater. Eng. Perform.* 2017;26:3560–8. <https://doi.org/10.1007/s11665-017-2768-6>.
- [42] Waqar S, Sun Q, Liu J, Guo K, Sun J. Numerical investigation of thermal behavior and melt pool morphology in multi-track multi-layer selective laser melting of the 316L steel. *Int. J. Adv. Manuf. Technol.* 2021;112:879–95. <https://doi.org/10.1007/s00170-020-06360-0>.
- [43] Dilip JJS, Zhang S, Teng C, Zeng K, Robinson C, Pal D, et al. Influence of processing parameters on the evolution of melt pool, porosity, and microstructures in Ti-6Al-4V alloy parts fabricated by selective laser melting. *Prog Addit Manuf* 2017;2: 157–67. <https://doi.org/10.1007/s40964-017-0030-2>.
- [44] Hüllermeier E, Waegeman W. Aleatoric and epistemic uncertainty in machine learning: An introduction to concepts and methods. *vol. 110*. Springer US; 2021. <https://doi.org/10.1007/s10994-021-05946-3>.
- [45] Possolo A. Simple guide for evaluating and expressing the uncertainty of NIST measurement results. *vol. 1900*. Washington, DC; 2015.
- [46] Cunningham R, Zhao C, Parab N, Kantzos C, Pauza J, Fezzaa K, et al. Keyhole threshold and morphology in laser melting revealed by ultrahigh-speed x-ray imaging. *Science* 2019;363:849–52. <https://doi.org/10.1126/science.aav4687>.
- [47] Oliveira JP, Santos TG, Miranda RM. Revisiting fundamental welding concepts to improve additive manufacturing: from theory to practice. *Prog. Mater. Sci.* 2020; 107:100590. <https://doi.org/10.1016/j.pmatsci.2019.100590>.
- [48] Bustillos J, Kim J, Moridi A. Exploiting lack of fusion defects for microstructural engineering in additive manufacturing. *Addit. Manuf.* 2021;48:102399. <https://doi.org/10.1016/j.addma.2021.102399>.
- [49] Li G, An Q, Duan B, Borgsmiller L, Al Malki M, Agne M, et al. Fracture toughness of thermoelectric materials. *Materials Science and Engineering: R: Reports* 2021;144: 1–12. <https://doi.org/10.1016/j.msere.2021.100607>.